International Journal of Microwave and Wireless Technologies

cambridge.org/mrf

Research Paper

Cite this article: Zhao C, Aslan Y, Garcia-Tejero A, Bouwmeester W, Yarovoy A (2025) Impact of misalignments with rotatable dihedral calibration target in mm-wave polarimetric MIMO automotive radar. International Journal of Microwave and Wireless Technologies, 1–12. https://doi.org/ 10.1017/S1759078725102468

Received: 31 January 2025 Revised: 8 October 2025 Accepted: 14 October 2025

Keywords:

calibration; dihedral scattering; MIMO radar; target misalignments; wave polarimetry

Corresponding author: Changxu Zhao; Email: c.zhao-2@tudelft.nl

© The Author(s), 2025. Published by Cambridge University Press in association with The European Microwave Association. This is an Open Access article, distributed under the terms of the Creative Commons Attribution licence (http://creativecommons.org/licenses/by/4.0), which permits unrestricted re-use, distribution and reproduction, provided the original article is properly cited.



Impact of misalignments with rotatable dihedral calibration target in mm-wave polarimetric MIMO automotive radar

Changxu Zhao¹, Yanki Aslan¹, Alejandro Garcia-Tejero², Wietse Bouwmeester³ and Alexander Yarovoy¹

¹Microelectronics, Delft University of Technology, Delft, Netherlands; ²Huber+Suhner AG, Herisau, Switzerland and ³Robin Radar Systems BV, The Hague, Netherlands

Abstract

The impact of misalignment errors, specifically yaw and pitch deviations, on dihedral reflectors' scattering responses is studied for millimeter-wave polarimetric multiple-input multiple-output automotive radars. Through simulations and experiments at 77 GHz, it is demonstrated that significant radar cross-section (RCS) variations of up to 30 dB can occur within small misalignment ranges (0°–2°). The findings emphasize that larger dihedral dimensions can amplify sensitivity to misalignment in some specific misalignment scenarios, offering trade-offs between reflection strength and robustness to misalignment errors. The study also explores near-field effects, revealing notable discrepancies between the dihedral near- and far-field scattering response in misalignment scenarios. A polarimetric calibration method is applied to show how polarimetric channel phase response is affected under such conditions, achieving stable results in specific configurations (e.g., dihedral at 0° under yaw misalignment angle). This study addresses key challenges in calibration accuracy, including the high sensitivity of RCS to small angular misalignments, the trade-offs between reflector dimensions and robustness, and the influence of near-field effects in practical setups.

Introduction

Multiple-input multiple-output (MIMO) antenna systems have become increasingly popular across various wireless applications, including communication networks, human monitoring, and automotive sensing. In [1], a MIMO antenna with wideband gain enhancement was proposed to reduce measurement errors in human respiratory monitoring. A dual-band MIMO smartphone antenna for 5G communications was introduced in [2], addressing the challenge of improving isolation among radiating elements. MIMO antenna designs for mmWave communications (24–38 GHz) have been presented in [3–5], emphasizing lightweight and easily realizable structures. In this paper, we focus on automotive polarimetric MIMO radars operating at millimeter-wave (mm-Wave) band (76–81 GHz) [6–8]. In those MIMO radars, single-polarized subarrays are utilized, which allow the radar systems to exploit the polarization scattering characteristics of targets and environments to extract valuable information. Applications of polarimetry are widely seen in weather radars [9], radio telescopes [10], and synthetic aperture radars [11]. More recently, polarimetric MIMO radars have gained attention in automotive applications, demonstrating significant potential for enhancing target detection [12, 13], classification [14, 15], and vehicle self-localization [16].

To maintain the accuracy and reliability of polarimetric measurements, proper calibration is essential [8]. Polarimetric calibration ensures that the system's inherent errors, such as channel imbalances [17] and polarization bias [18], are minimized, providing trustworthy data on the target's polarimetric scattering matrix for downstream processing. Corner reflectors are often used for radar calibration. In [19], a large number of trihedral corner reflectors are employed as calibration targets, providing a cost-effective solution for integration into road infrastructure in real-life scenarios to monitor the radar state. On the other hand, dihedral corner reflectors are commonly used as reference targets for polarimetric radar calibration [12, 17, 20]. Their well-defined and predictable scattering behavior, influenced by angular positioning, which can be controlled by the angle of orientation with respect to the radar, makes them ideal for this purpose. In most calibration procedures utilizing a dihedral corner reflector, the dihedral self-rotation angle is commonly considered to change its polarization property. In practice, misalignment between the dihedral and the radar during the measurement can lead to a reduction in received scattering power and unexpected errors in the measured polarimetric scattering

coefficients (amplitude and phase) of targets. Therefore, it is essential to study and understand the radar cross-section (RCS) variation of the dihedral when there is misalignment between the dihedral and the radar. In addition, although far-field scattering is considered for most dihedral measurements, near-field scattering of dihedral becomes particularly relevant in practical scenarios, such as outdoor measurements where larger dihedral dimensions are used to boost the signal-to-noise-ratio (SNR), thereby pushing the far-field distance beyond feasible limits; or in constrained environments like anechoic chamber, where the measurement setup remains within the near-field of the reflector.

The research on dihedral far-field RCS computation via analytical expressions has been done in many studies. [21] and [22] have explored analytical and simplified models for evaluating the RCS of dihedral corner reflectors. In [21], a compact formula was derived for arbitrary aspect angles, but the analysis assumes a fixed dihedral self-rotation angle. Extending this formula to an arbitrary self-rotation angle would require additional terms to account for geometric rotation and coordinate transformation, which were not addressed. Similarly, [22] proposed a simplified RCS model considering incident angle variations, but did not examine the effect of dihedral self-rotation, which is commonly used in polarimetric measurement. While both works provide methods to evaluate dihedral far-field RCS, they do not quantify the impact of misalignment errors (e.g., yaw and pitch) on the RCS response, nor do they investigate how the physical dimensions of the dihedral influence robustness to such misalignments. In the mm-wave band, which is prevalent in modern automotive radar, the RCS reduction of the dihedral becomes even more sensitive to the misalignment errors due to the smaller wavelength. These misalignment-induced RCS reductions can introduce significant uncertainties, complicating the calibration process. In [17], the dihedral RCS reduction caused by the yaw angle misalignment between the dihedral and the radar was studied under the mm-wave band for the automotive radar. However, the research in [17] was limited in both the dihedral dimensions (only three sizes were considered) and the amount of misalignment studied (within 1.5°). Besides, the study in [17] was restricted to yaw misalignment errors and the near-field scattering of the dihedral.

This paper addresses the need for a comprehensive understanding of dihedral scattering measurements for polarimetric automotive radars calibration in the presence of misalignment errors through a novel investigation of the scattering behavior of dihedral corner reflectors under misalignment errors at 77 GHz. Both simulation and measurement results are utilized to analyze these effects. As an extension of the work presented in [8], which assumes ideal radar-target alignment, this paper studies calibration target misalignment effects in measured amplitude-phase responses and further explores polarimetric phase calibration by analyzing the target's polarimetric scattering response under misalignment errors. These findings are critical for extending polarimetric measurements and calibration beyond controlled environments, such as anechoic chambers, where misalignment between the radar and the targets is more likely. The polarimetric phase calibration technique introduced in [8] is applied here to examine how misalignment errors influence the target's polarimetric phase variation. The major contributions from this research are listed below:

- First-time analysis of dihedral self-rotation and dimension effects on misalignment (yaw and pitch).
- First-time practical validation of yaw misalignments in 77 GHz polarimetric MIMO radar, in particular in the near field.

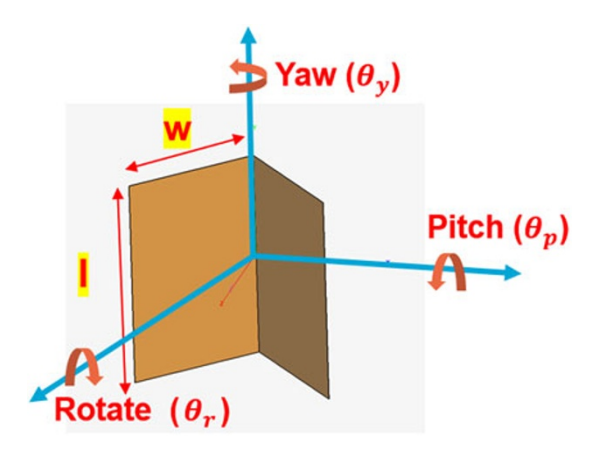


Figure 1. Dihedral dimensions and motions definition: yaw, pitch, and rotate.

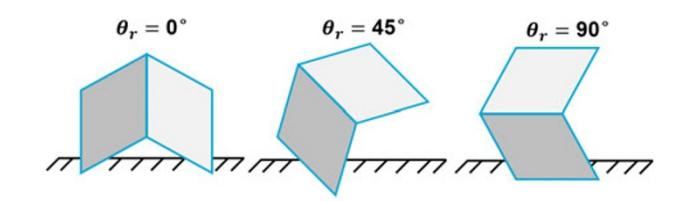


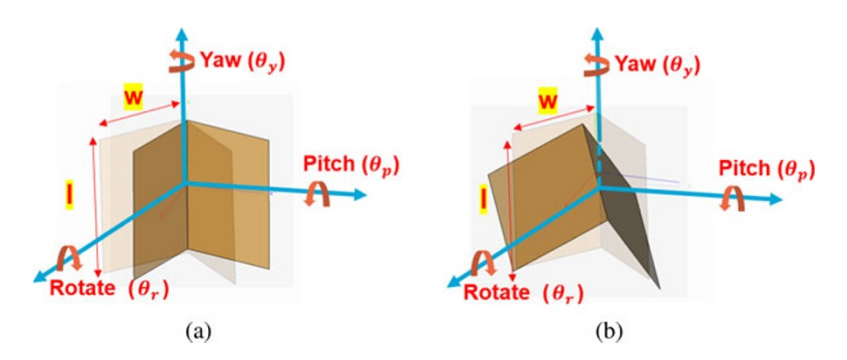
Figure 2. Dihedral self-rotation (θ_r) .

- Novel insights and recommendations on dihedral target dimensions for robustness against the misalignment errors.
- First-time study of the effect of misalignment errors in polarimetric phase response.

The remainder of this paper is organized as follows: Section 2 details the theoretical background. Section 3 describes the simulation setup and the results of the dihedral scattering under yaw and pitch misalignment errors. Section 4 presents the measurement results. Section 5 will discuss the implications for polarimetric phase calibration. Finally, Section 6 concludes the paper.

Theory of polarimetric scattering from a dihedral

The RCS of the dihedral can be calculated using Eq. (1) assuming a far-field scattering condition, where w and l represent the width (w) and length (l) of the dihedral, respectively, as illustrated in Fig. 1. The target scattering matrix is defined in Eq. (2) under H-V polarization basis, whereas its components are known as complex scattering amplitudes. The first column of S is measured by transmitting a horizontally polarized wave and employing two antennas horizontally and vertically polarized to record the scattered waves. The second column is measured in the same form but transmitting a vertically polarized wave. The polarimetric scattering matrix of the dihedral, expressed in Eq. (3) under H-V polarization basis, is a function of its angular orientation, with θ_r denoting the rotation angle. This angular dependence is a key characteristic of dihedral reflectors, making them a widely preferred reference target in polarimetric radar calibration due to their well-defined and predictable polarimetric scattering behavior. As shown in Fig. 2, the self-rotation of the dihedral allows precise measurement of both co- and cross-polarized components using a fully polarized antenna. For instance, in a radar system equipped with an H-V polarized antenna, the dihedral can be oriented at $\theta_r = 0^o$ and $\theta_r = 45^{\circ}$ to capture the co- and cross-pol responses, respectively.



30 9.5 GHz 77 GHz 10 0 1 2 3 4 5 Yaw angle [deg]

Figure 4. Simulated $90^{\rm o}$ oriented dihedral scattering RCS with yaw misalignment under two different frequencies.

In practice, measurement setups are often subject to alignment errors between the radar and the dihedral, including possible yaw (θ_y) and pitch (θ_p) angles, as defined in Fig. 1 and shown in Fig. 3.

To illustrate the consequences of misalignment, Fig. 4 shows the simulated RCS of a 90° oriented dihedral, with dimensions 135 mm x 180 mm (w x l), under different yaw misalignment angles, assuming plane wave incidence. At 9.5 GHz, the RCS variation with yaw angle is modest. However, at 77 GHz, the RCS changes sharply by approximately 25 dB between 0° and 2°. Such a degree of yaw angle misalignment can occur easily if the radar and the dihedral are not precisely aligned during the experiment [17, 22].

This significant sensitivity at higher frequencies, such as 77 GHz or beyond, underscores the importance of studying the dihedral scattering behavior under misalignment errors to ensure accurate radar calibration. Due to the increased analytical complexity of dihedral RCS modeling under misalignment errors, especially when both far-field and near-field are needed to be considered, numerical simulations by full-wave tools like FEKO, with accompanying measurements, are preferred [17].

$$\sigma_{DH} = \frac{8\pi w^2 l^2}{\lambda^2} \tag{1}$$

$$S = \begin{bmatrix} S_{11} & S_{12} \\ S_{21} & S_{22} \end{bmatrix} = \begin{bmatrix} S_{hh} & S_{h\nu} \\ S_{\nu h} & S_{\nu \nu} \end{bmatrix}$$
 (2)

$$S_{DH}(\theta_r) = \sqrt{\frac{\sigma_{DH}}{4\pi}} \begin{bmatrix} -\cos 2\theta_r & \sin 2\theta_r \\ \sin 2\theta_r & \cos 2\theta_r \end{bmatrix}$$
(3)

Figure 3. Yaw (θ_y) and pitch (θ_p) angle variation when $\theta_r=0^o$. (a) Pitch angle variation.

Dihedral scattering simulation under misalignment errors

The simulations discussed in this section were performed in Altair FEKO simulation software at 77 GHz. The details of the simulation setup and the results will be discussed in the following subsections.

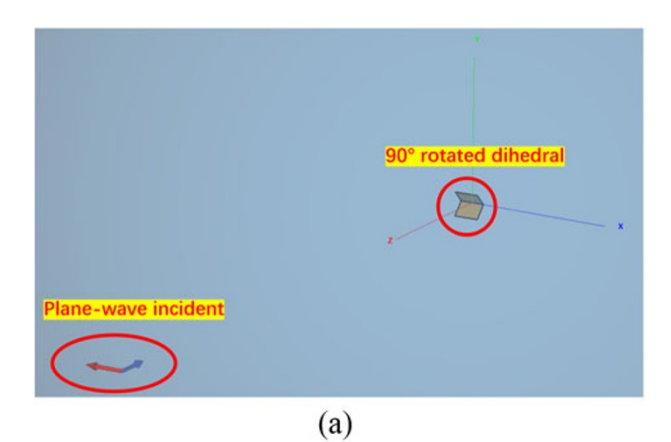
Full-wave simulation model

The dihedral corner reflector was modeled in FEKO, as illustrated in Fig. 1, for which the dimensions (w and l) can be varied during the simulation. The material selected for the dihedral simulations was a perfect electric conductor with zero thickness for simulation efficiency. The far-field distance of the target can be calculated using $\frac{2D^2}{\lambda}$, where D represents the largest dimension of the target. The dihedral mentioned above has a far field of approximately 40 m.

Two simulation setups were employed, differing in the type of source used. For both setups, the Multilevel Fast Multipole Method solver was used instead of the normal Method of Moments solver, as it shortens the simulation time for the electrically large target, like the dihedral used here. The polarization states of the incident wave for both setups are horizontally polarized. The first setup utilized a plane-wave source, as shown in Fig. 5(a), enabling simulation under strict far-field conditions. This setup was used to analyze the dihedral's far-field scattering behavior under yaw and pitch misalignment. The second setup addressed a practical limitation: during measurements under 77 GHz, the radar-to-dihedral distance was restricted to 3.6 m, sufficient for achieving far-field conditions for the radar, but insufficient for achieving far-field conditions for a dihedral with fixed dimensions (140 mm in width and 200 mm in length) used during the measurement.

To simulate the near-field effects efficiently, a 1x11 horizontally polarized ideal dipole array was introduced as the source [23], as depicted in Fig. 6, which mimicks the pattern of the radar under test at the two orthogonal cutplanes around the main lobe and can be replaced by any other 3D pattern data based on the radars or sensing requirements. The element number was selected as a trade-off between simulation accuracy and time. Horizontal polarization was selected to be comparable with the polarization state used in the first simulation setup. The dipole array's radiation pattern, shown in Fig. 7, offers a wide beamwidth ($\pm 40^{\circ}$ at 3 dB) in azimuth and a narrow beam in elevation, a configuration common in automotive sensing [6, 24, 25], to be comparable with the MIMO automotive radar used in the measurement later. By using the Taylor amplitude tapering to the array, -28 dB sidelobe level and 109 dB cross-polarization isolation were achieved.

The dipole array's radiation pattern was first simulated in isolation, with the dihedral absent, and the results were exported as



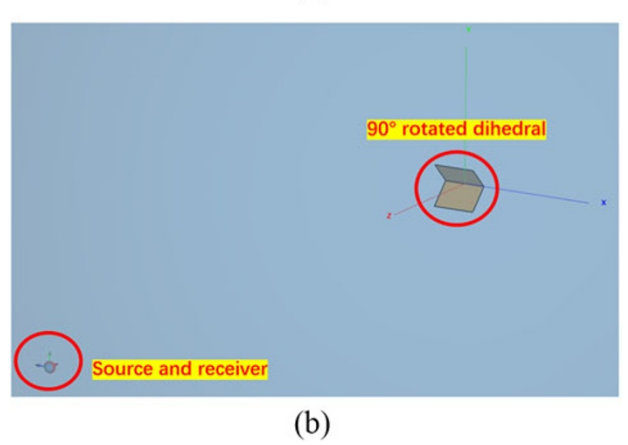


Figure 5. FEKO simulation set-up. (a) Simulation setup 1: Plane wave incidence. (b) Simulation setup 2: Spherical mode source and far-field receiving antenna.

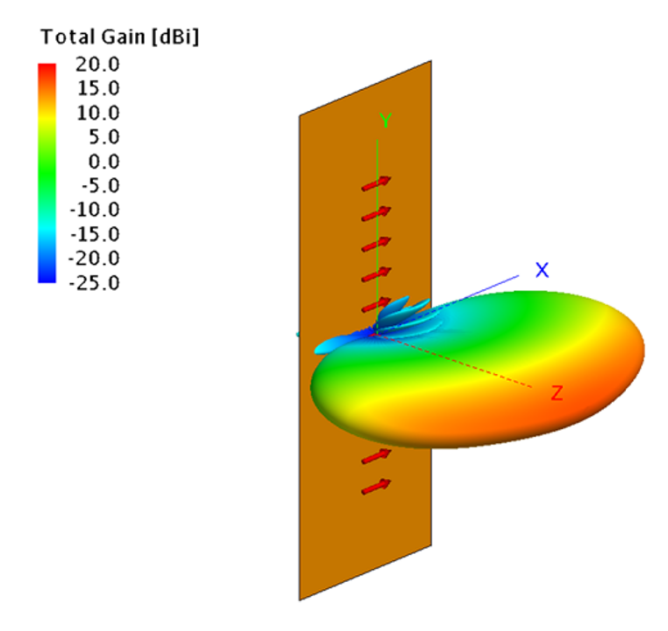


Figure 6. An equivalent subarray model with 1x11 dipole array in FEKO, mimicking the pattern of the radar under test in both $\Phi=0^\circ$ and $\Phi=90^\circ$ cuts around the main beam.

spherical mode (.sph) and far-field (.ffe) files. In the second setup of the dihedral scattering simulation, depicted in Fig. 5(b), the spherical mode file was used as the source, while the far-field file

was applied to the receiving antenna. Both the source and receiving antenna were co-located, with their distance from the dihedral adjustable for simulation in both near- and far-field.

The complete flow of simulation, including both simulation setups, is presented in Fig. 8. The simulation was performed on a server equipped with 256 G bytes of RAM and two Intel Xeon-Gold 2.1 GHz/20-core Processors. The time cost for a complete simulation round using the first setup is 3.3 min, while for the second setup, the simulation time increased to 5.7 min. It can be seen that by replacing the plane-wave source with the spherical mode source and the far-field receiving antenna, the simulation time has increased by 72%.

Results of yaw misalignment in far-field

In this subsection, the effect of yaw misalignment for varied dihedral dimensions on dihedral far-field RCS will be discussed. The simulation was divided into four sets:

- (i) The dihedral was rotated to 90° , and the width was fixed at 135 mm. Then, for each length from 50 mm to 180 mm, the RCS was simulated under yaw angles from 0° to 5° .
- (ii) The dihedral was rotated to 90° , and the length was fixed at 180 mm. Then, for each width from 50 mm to 180 mm, the RCS was simulated under yaw angles from 0° to 5° .
- (iii) The dihedral was rotated to 0°, and the width was fixed at 135 mm. Then, for each length from 50 mm to 180 mm, the RCS was simulated under yaw angles from 0° to 5°.
- (iv) The dihedral was rotated to 0°, and the length was fixed at 180 mm. Then, for each width from 50 mm to 180 mm, the RCS was simulated under yaw angles from 0° to 5°.

To obtain the general trend of the far-field RCS variation and control the simulation time, a step of 1^{o} was selected for yaw angle scanning from 0^{o} to 5^{o} in all four simulation sets. The scanning steps were then finer in the chosen ranges of yaw angle as shown in Fig. 14 to capture the local details of the far-field RCS variation. The sizes of the dihedral during the simulation were selected to balance the simulation time and the strength of the dihedral backscattered power.

Figure 9 shows the case (i) of simulation results. Despite the dihedral with a larger dimension having a larger RCS at 0° yaw angle, its RCS can drop even to a lower level than the dihedral with a smaller dimension when the yaw angle increases. For example, the dihedral with 110 mm length initially has RCS equal to 25 dB drop, but then drops to 2 dB when the yaw angle increases to 1°. In contrast, the initial RCS of the dihedral with 50 mm length is 18 dB, and it only drops 3 dB after the yaw angle increases to 1°. Therefore, when the dihedral is rotated to 90°, its RCS dependency on the change of yaw angle strongly varies with the change of length of the dihedral.

The case (ii) of simulation results is shown in Fig. 10. When the dihedral is rotated to 90°, compared with varying dihedral length, the change in dihedral width does not affect the dependency between the RCS variation and the yaw angle. Instead, the increase in dihedral width only affects the overall RCS. The cases (iii) and (IV) of simulation results are shown in Fig. 11 and Fig. 12. It is observed that when the dihedral is rotated to 0°, either length or width variation will not affect the dependency of the change of RCS on the varying yaw angle. And now the RCS has become stable under the yaw angle misalignment (both near and far field compatible).

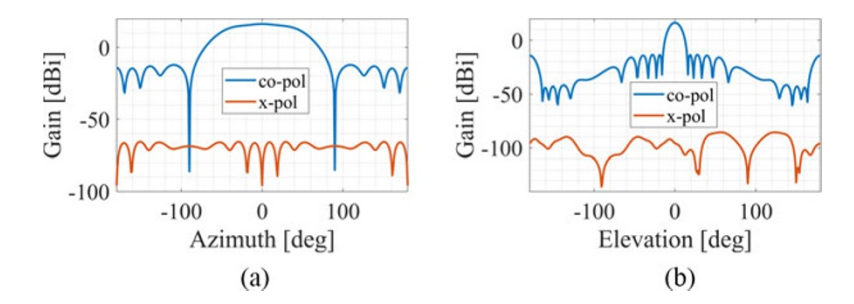


Figure 7. Patterns of an equivalent subarray, mimicking the pattern of the radar under test. (a) $phi = 0^{\circ}$ cut (b) $phi = 90^{\circ}$ cut

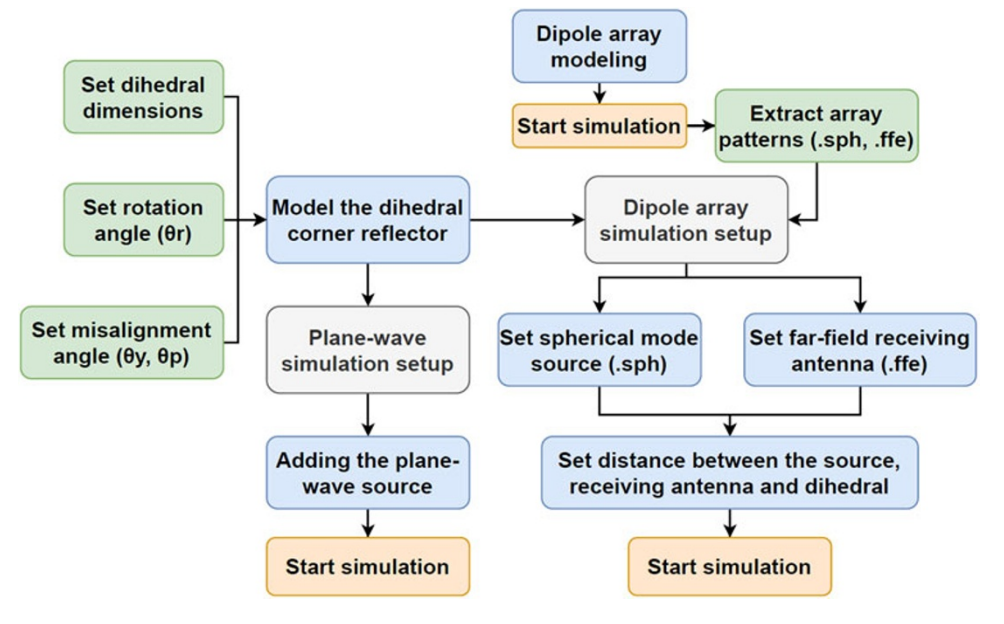


Figure 8. Simulation flow chart

Figure 13 illustrates the simulated far-field scattering patterns of a dihedral rotated by 90° ($\theta_r = 90^{\circ}$) for different dihedral lengths. When observed at 0° azimuth, the RCS consistently increases with the dihedral length. However, in the presence of yaw misalignment, as depicted in Fig. 13(b), the RCS at 0° azimuth is influenced by the side lobes and nulls in the dihedral's scattering patterns. These variations in the side lobes and nulls are directly reflected in the changes in RCS due to yaw misalignment.

In order to further investigate the influence of the yaw angle on the RCS variation when the dihedral is at 90° , Fig. 14 shows the same results as Fig. 9 but with 0.1° simulation step of yaw angle between 0° to 1° and 2° to 3° . After simulating with 0.1° yaw angle step, the RCS variation oscillation can be observed between 0° to 1° and 2° to 3° yaw angles. By utilizing the null positions among those oscillations, initial misalignment correction between the radar and the dihedral can be done to avoid no backscattering signal at the null positions, even for an electrically large target.

Overall, it is observed that when yaw angle misalignment is introduced, and the dihedral is rotated to 90°, the change of the dihedral RCS can range from 20 dB to 30 dB within 0° to 5° yaw angle. The amount of RCS change can also depend on the length of the dihedral. Due to the null position of the dihedral far-field scattering pattern, the most rapid change of RCS within 0° to 1° is observed when the length of the dihedral is equal to 120 mm,

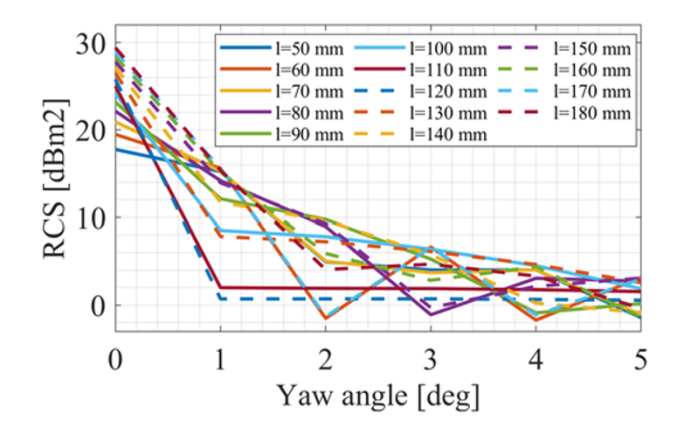


Figure 9. 90° rotated Dihedral RCS simulation under different yaw angles and varying dihedral length.

which should be avoided, while the smallest change happens when the length of the dihedral is equal to 50 mm. By carefully selecting the length of the dihedral, the trend of the RCS change can be controlled within a specific range of yaw angle misalignment. Based on the simulation setup when $\theta_r = 90^\circ$, it is recommended to select w = 135 mm and l = 50 mm when the yaw misalignment can be controlled within 1°; if the measurement setup does not allow

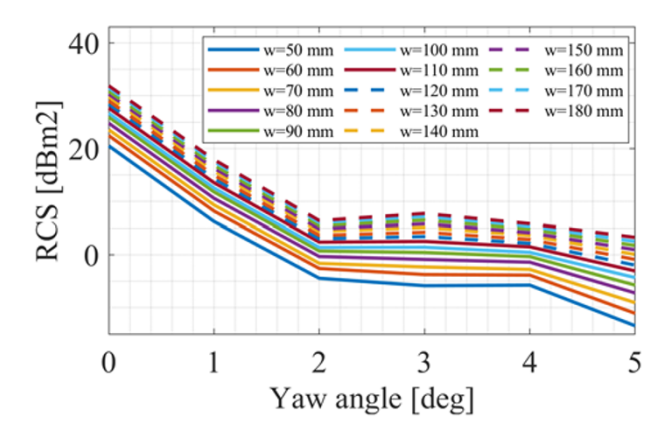


Figure 10. 90° rotated Dihedral RCS simulation under different yaw angles and varying dihedral width.

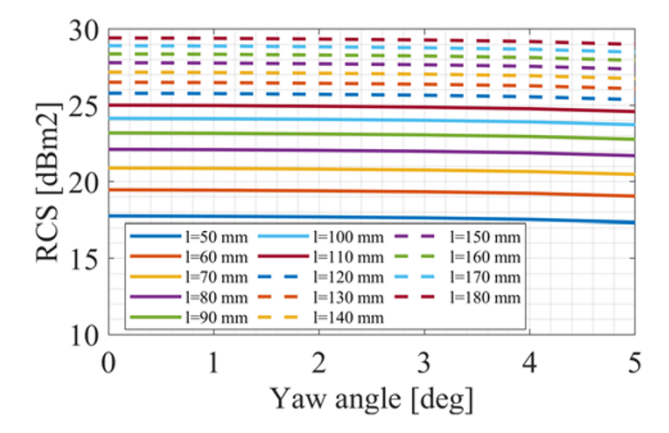


Figure 11. 0° rotated Dihedral RCS simulation under different yaw angles and varying dihedral length.

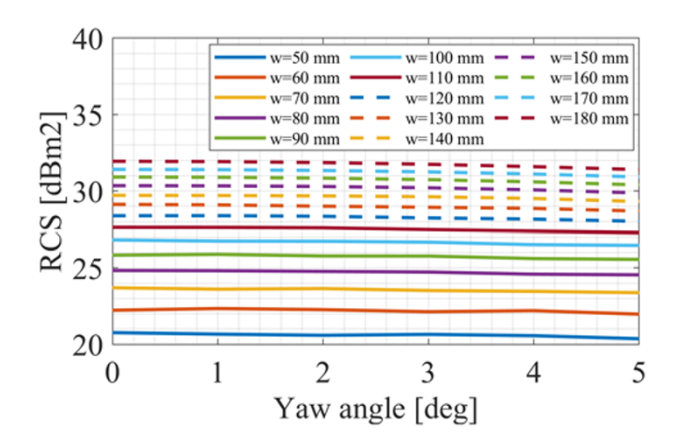


Figure 12. 0° rotated Dihedral RCS simulation under different yaw angles and varying dihedral width.

small yaw misalignment within 1°, then it is recommended to use the dihedral with w=135 mm and l=100 mm or w=135 and l=130 mm to obtain stable RCS under large yaw misalignment angles. On the other hand, when the dihedral is rotated to 0°, the RCS becomes stable within 0° to 5° yaw angle. Both length and width variations of the dihedral only affect the overall RCS value.

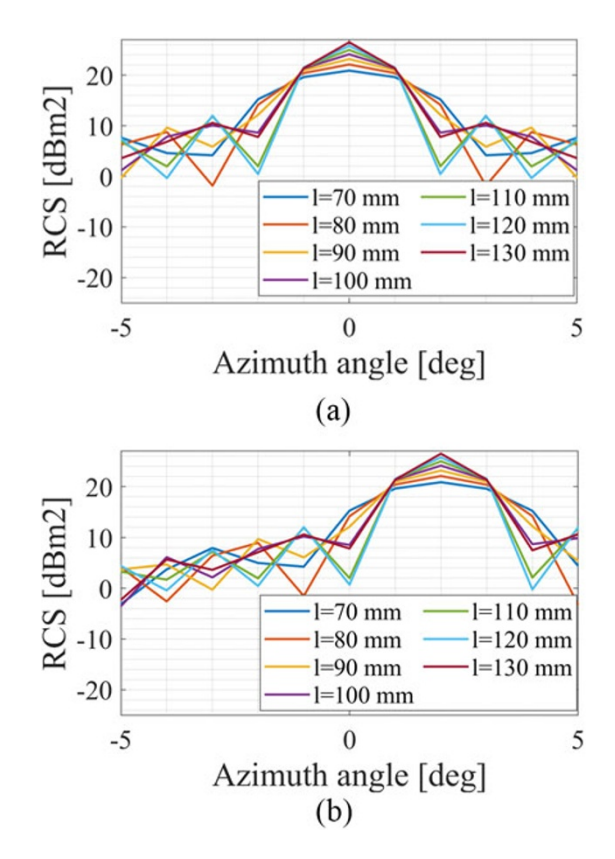


Figure 13. Dihedral scattering pattern under varying dihedral length and $\theta_r=90^o$. (a) $\theta_y=0^o$ (b) $\theta_y=1^o$

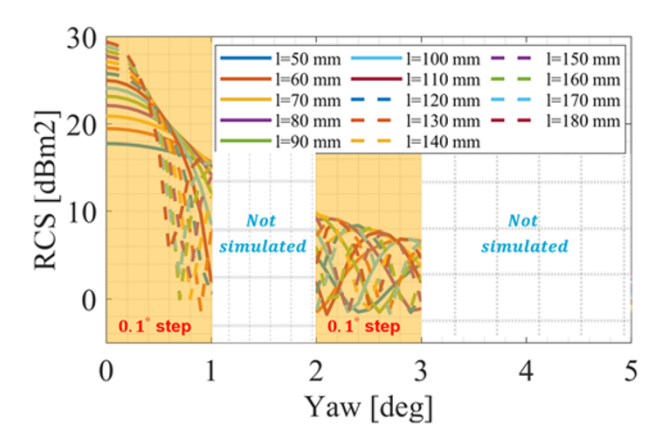


Figure 14. 90° rotated Dihedral RCS simulation under different yaw angles and varying dihedral length (with 0.1° yaw angle step between 0° to 1° and 2° to 3°).

Results of pitch misalignment in far-field

Same as the yaw angle simulation, the pitch misalignment simulation was also analyzed under four different sets:

- (i) The dihedral was rotated to 90°, and the width was fixed at 135 mm. Then, for each length from 50 mm to 180 mm, the RCS was simulated under pitch angles from 0° to 5°.
- (ii) The dihedral was rotated to 90°, and the length was fixed at 180 mm. Then, for each width from 50 mm to 180 mm, the RCS was simulated under pitch angles from 0° to 5°.

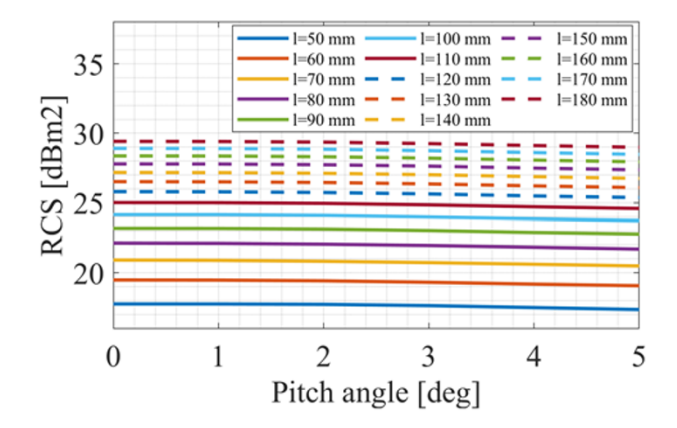


Figure 15. 90° rotated Dihedral RCS simulation under different pitch angles and varying dihedral length.

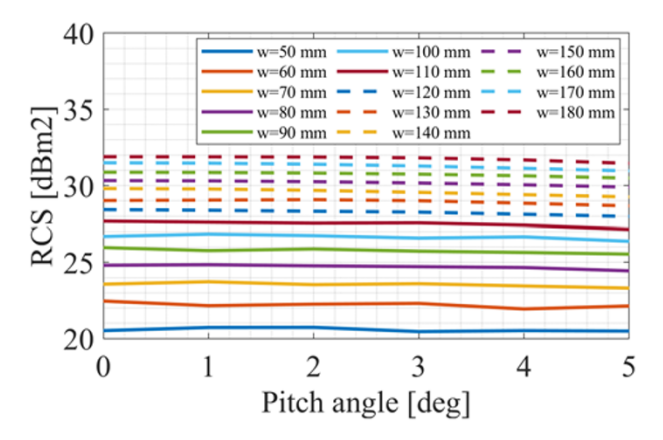


Figure 16. 90° rotated Dihedral RCS simulation under different pitch angles and varying dihedral width.

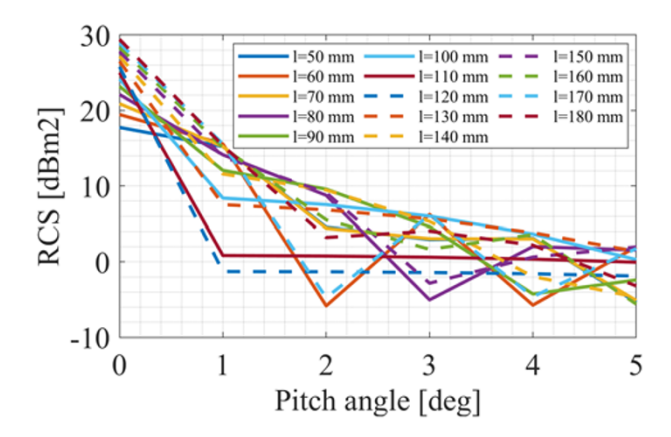


Figure 17. 0° rotated Dihedral RCS simulation under different pitch angles and varying dihedral length.

- (iii) The dihedral was rotated to 0°, and the width was fixed at 135 mm. Then, for each length from 50 mm to 180 mm, the RCS was simulated under pitch angles from 0° to 5°.
- (iv) The dihedral was rotated to 0°, and the length was fixed at 180 mm. Then, for each width from 50 mm to 180 mm, the RCS was simulated under pitch angles from 0° to 5°.

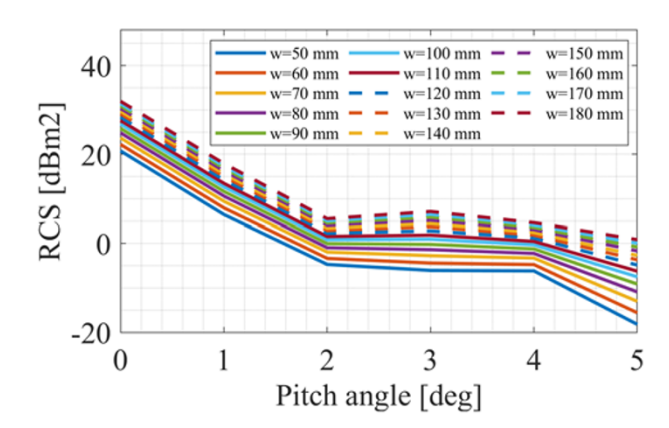


Figure 18. 0° rotated Dihedral RCS simulation under different pitch angles and varying dihedral width.

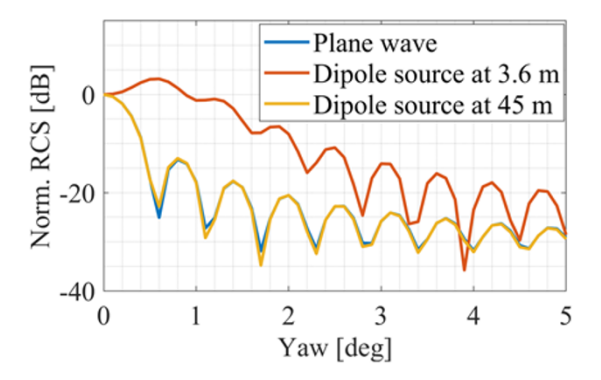


Figure 19. Simulation results comparison between plane wave and dipole source incidence at two distances ($\theta_r=90^{\circ}$).

During the simulation, the step of pitch angle scanning was set to 1^{o} . As mentioned before, the sizes of the dihedral during the simulation were selected to balance the simulation time and the strength of the dihedral backscattered power.

The simulation results of case (i) and case (ii) are shown in Fig. 15 and Fig. 16. It is observed that when the dihedral is rotated to 90°, changing the pitch angle will not affect the RCS value. Besides, both length and width variation here can only influence the overall RCS value. When the dihedral is rotated to 0°, the pitch angle starts to affect the RCS value. The change of RCS at different pitch angles when the dihedral is rotated to 0° can be seen from Fig. 17. In addition, changing the length of the dihedral can affect the trend of the RCS change. Figure 18 shows that when the dihedral is rotated to 0°, changing the width of the dihedral will only influence the overall RCS value.

From the above analysis, it can be seen that including 0^o to 5^o pitch angle misalignment can already lead to a significant change in dihedral RCS and cause the overall RCS drop for about 20 dB to 30 dB when the dihedral is rotated to 0^o . The length of the dihedral can influence the trend of the RCS change. Based on the simulation setup when $\theta_r = 0^\circ$, it is recommended to select w = 135 mm and l = 50 mm when the pitch misalignment can be controlled within 1° ; if the measurement setup does not allow small pitch misalignment within 1° , then it is recommended to use the dihedral with w = 135 mm and l = 100 mm or w = 135 and l = 130 mm to obtain stable RCS under large pitch misalignment angles. On the other hand, when the dihedral is rotated to 90^o , the

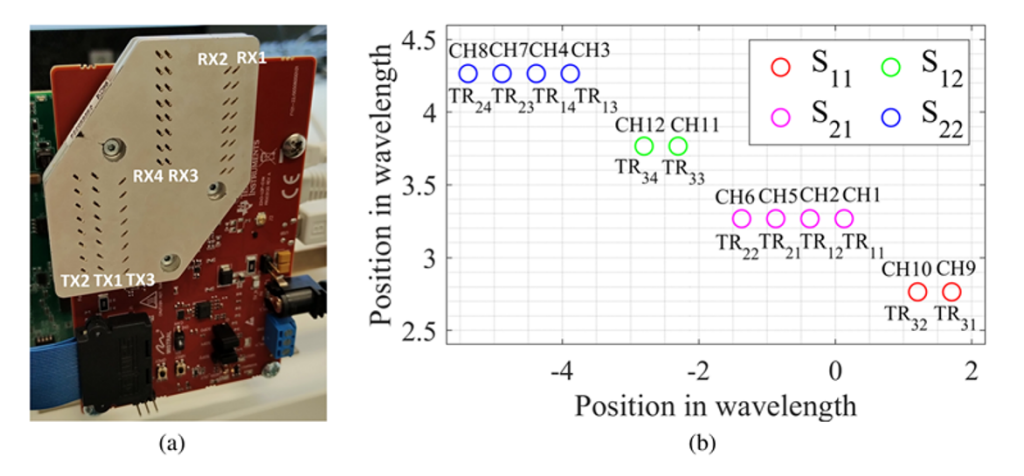


Figure 20. Radar under test [8]. (a) MIMO topology (b) Polarimetric virtual array

RCS becomes stable within 0° to 5° pitch angle misalignment. Here, both changes of dihedral length and width only affect the overall RCS value. Comparing the results from yaw and pitch misalignment angles, it can be seen that the simulations between 0° and 90° are symmetrical and vice versa. As an example, the change in the RCS of a 90° orientated dihedral with varying yaw angle and dihedral length can be derived from the change in the RCS of a 0° dihedral with varying pitch angle and dihedral length. This symmetry simplifies the derivation of the RCS variation of a dihedral caused by the two types of misalignment angles (θ_v and θ_p).

Discussion on the near-field effects

The near-field scattering response of the dihedral was simulated using the second setup described in the previous section. Figure 19 compares the simulation results obtained with a plane wave source and those using the dipole array source. For these simulations, the dihedral dimensions were fixed at 140 mm in width and 200 mm in length, consistent with the size used in subsequent practical measurements.

The far-field distance for the dihedral with dimensions 140 mm x 200 mm (w x l) is approximately 42 meters. Accordingly, the simulation results using a plane wave closely matched the results obtained when the dipole array source was placed 45 meters away, as shown in Fig. 19, confirming far-field conditions. In contrast, placing the dipole source 3.6 meters from the dihedral will result in the near-field measurement, which coincides with the distance used between the dihedral and the radar during the actual measurement.

As shown in Fig. 19, the RCS difference between the near-field and far-field simulations is approximately 13 dB within the yaw angle range from 0.5° to 2°, and drops to 5 dB when the yaw angle is increased. This discrepancy highlights the significant impact of near-field conditions on the dihedral's scattering response.

Measurement of dihedral scattering under yaw misalignment error

To validate the simulation results, practical measurements have been done using the 77 GHz MIMO radar and the dihedral inside the anechoic chamber. The detailed measurement setup and results are discussed in the following subsections.

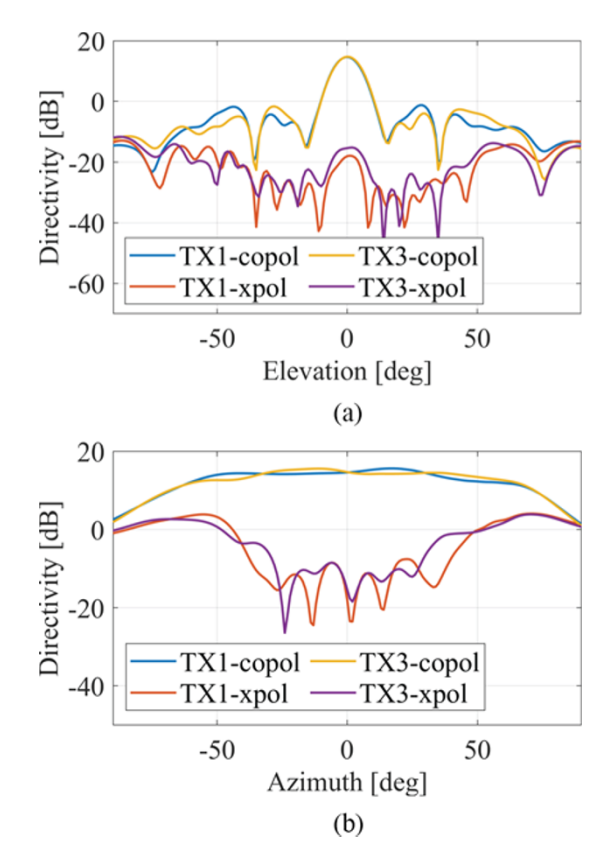


Figure 21. TX1 (+45°) and TX3 (-45°) subarray simulated radiation pattern [8]. (a) $phi=90^{\circ}$ cut (b) $phi=0^{\circ}$ cut

Measurement set-up and radar under test

This research utilizes a $\pm 45^o$ polarized MIMO automotive radar operating in the 77 GHz band, designed by HUBER+SUHNER AG. The radar measures the polarimetric scattering matrix, represented by Eq. (4), while the DH scattering matrix under slant polarization basis is shown in Eq. (5). The RF front end includes an MMIC [26] with four receivers, three transmitters directly connected to a metalized plastic waveguide antenna manufactured using a novel combination of 3D printing and metallization processes developed by HUBER+SUHNER AG [27]. The antenna

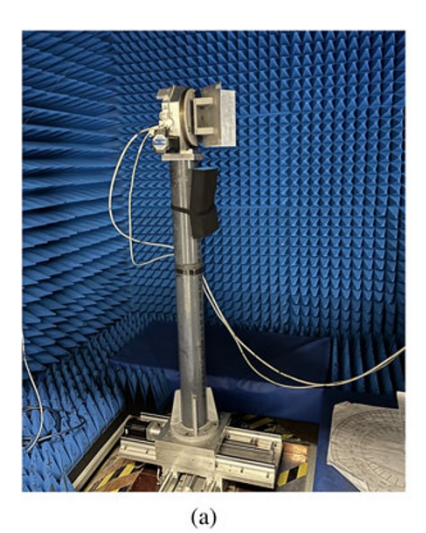




Figure 22. Measurement setup in the anechoic chamber. (a) Dihedral setup (b) Radar setup

is mounted on top of the printed circuit board, as shown in Fig. 20(a). The physical antenna channels are strategically positioned to achieve a fully populated virtual array with $\lambda/2$ spacing between the four polarimetric channels (S11, S12, S21, S22), as depicted in Fig. 20(b).

The radar incorporates two subarray types, each offering orthogonal slant polarizations ($\pm 45^{\circ}$). These subarrays are based on a linear array of eight open-ended waveguides [28]. Simulated radiation patterns for transmitter 1 and transmitter 3 are presented in Fig. 21. The subarrays achieve an elevation ($phi = 90^{\circ}$) 3-dB field-of-view (FOV) of 9.1° and an azimuthal ($phi = 0^{\circ}$) FOV of 105°, with a gain around 15 dBi. The cross-polarization discrimination reaches 35 dB at boresight, decreasing to 5 dB at 60° in the azimuthal plane, due to the inherent geometry of the array.

The measurement during this research was performed in the Delft University Chamber for Antenna Tests. A 140 mm x 200 mm dihedral corner reflector was used as the target and placed on a rotatable stand that has two motors that can provide both azimuth rotation and dihedral self-rotation, as shown in Fig. 22(a). The RUT was fixed during the measurement as shown in Fig. 22(b). The distance between the RUT and the dihedral was set to 3.6 m.

$$S_{\pm 45^{\circ}basis} = \begin{bmatrix} S_{11} & S_{12} \\ S_{21} & S_{22} \end{bmatrix} = \begin{bmatrix} S_{+45+45} & S_{+45-45} \\ S_{-45+45} & S_{-45-45} \end{bmatrix}$$
(4)

$$S_{DH_{slant}}(\theta_r) = \sqrt{\frac{\sigma_{DH}}{4\pi}} \begin{bmatrix} \sin 2\theta_r & \cos 2\theta_r \\ \cos 2\theta_r & -\sin 2\theta_r \end{bmatrix}$$
 (5)

Measurement results

Due to the limitation of the measurement equipment, only the yaw misalignment measurement was done. Figure 23 shows the measurement results, represented by the dashed lines. For comparison, the simulation result is included for $\theta_r=90^{\rm o}$ in both near-(source at 3.6 m) and far- (source at 45 m and plane wave incident) field, represented by the solid lines; both the measurement and the simulation were done with the $0.1^{\rm o}$ step when scanning the yaw angle. The results are normalized at $0^{\rm o}$ yaw angle. Each result was normalized according to its own maximum.

It can be seen from Fig. 23 that when the dihedral is rotated to 0° , the received power is stable over the yaw misalignment angle, as expected according to the simulation results. The overall variation of the received power is within 1 dB. In contrast, when the dihedral is rotated to 90° , the received power dropped for about 30 dB when the yaw angle reached 5° . By comparing the measured results at $\theta_r = 90^{\circ}$ and the corresponding simulated results at near-field, it can be verified that the dihedral was measured in its near-field during the measurement.

From the measurement result of the 90^o rotated dihedral and the corresponding simulation result in the near-field, it can be observed that there is an overall mismatch between the measured (red dashed curve) and the simulated (purple solid curve) results. In order to better observe this mismatch, the simulation range was extended to $\theta_y = -2^o$ and compared with the measured result from $\theta_y = 0^o$ to 5^o as shown in Fig. 24. After shifting the entire measured curve 0.6^o to the left, the measured and the simulated results are well-matched as shown in Fig. 24. This overall shift in the curve comes from the moving precision of the step motor that controls the yaw angle scanning.

Impact of misalignment errors in polarimetric phase response calibration

Calibration method

The calibration performed in this subsection aims to accurately obtain the polarimetric phase difference between the polarimetric scattering matrix coefficients for better target characterization.

The calibration method used during this research is extended from the method proposed in [8], where the calibration matrix was introduced, which can be directly multiplied by the raw radar data for the polarimetric phase calibration.

The raw measurement data consists of a 12x750x16x20 complex 4-D matrix, where 12 represents the number of channels, 750 is the number of samples per chirp, 16 denotes the number of chirps per frame, and 20 signifies the number of frames.

To obtain the reference data for calculating the calibration matrix, the measurement of the dihedral was done at $\theta_r = 45^o$ and $\theta_r = 0^o$, both without any misalignment angle ($\theta_y = \theta_p = 0^o$). The co-pol reference data was obtained from the measurement at

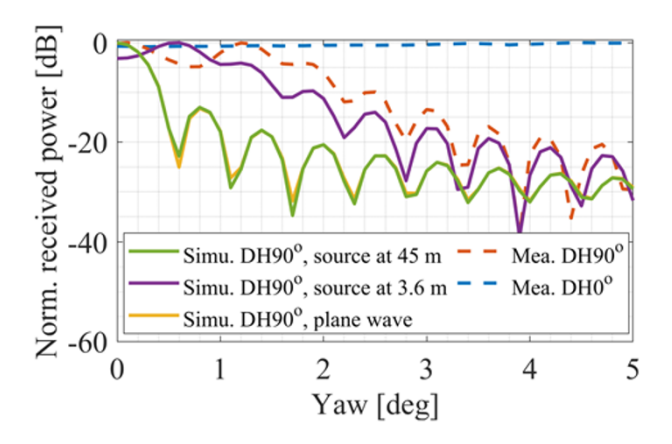


Figure 23. Measurement (dashed-line) and simulation (solid-lines) results comparison under yaw misalignment angle.

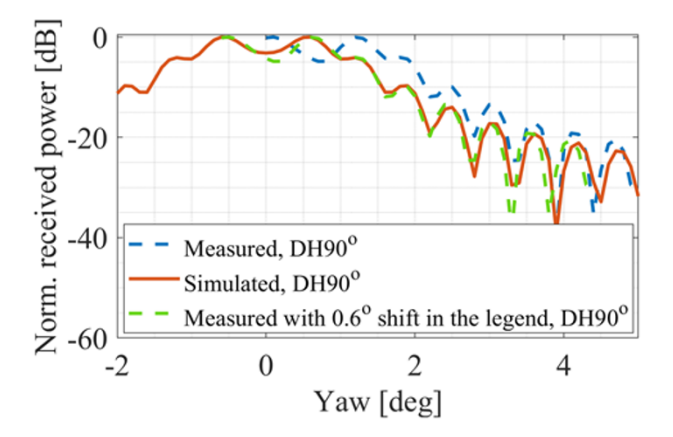


Figure 24. Misalignment between the measured and simulated results when $\theta_r = 90^o$.

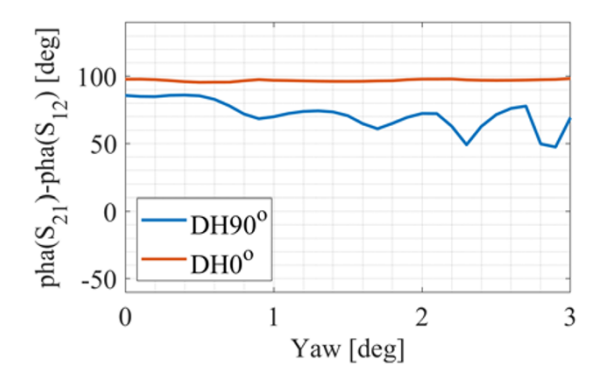


Figure 25. Uncalibrated cross-pol polarimetric phase difference from the measurement.

 $\theta_r=45^o$, and the cross-pol reference data was obtained from the measurement at $\theta_r=0^o$. The calibration matrix was calculated using the method proposed in [8] and then applied to the measured data when the yaw angle was present. The polarimetric channels' phase difference was calculated between S_{12} and S_{21} . According to the scattering matrix of the dihedral under $\pm 45^o$ polarimetric basis, the polarimetric phase difference between the cross-pol channels S_{12} and S_{21} should be 0^o when the dihedral is rotated to $\theta_r=0^o$ and $\theta_r=90^o$.

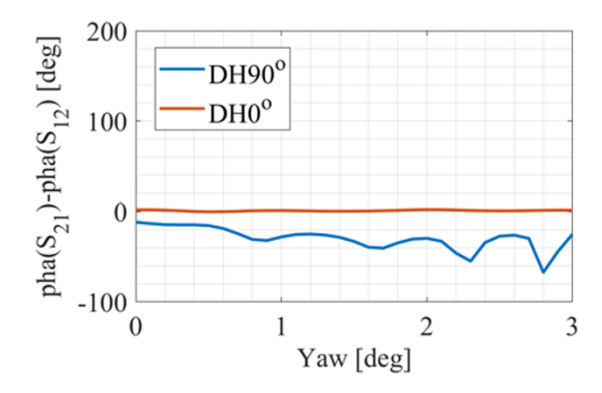


Figure 26. Calibrated (under no misalignment assumption) cross-pol polarimetric phase difference from the measurement.

Yaw angle misalignment errors

The uncalibrated polarimetric phase differences of the measured data are shown in Fig. 25, while the calibrated results are presented in Fig. 26. After calibration, the polarimetric phase difference for the 0° rotated dihedral stabilizes around 0^{o} , with a mean value of 1.2° and a standard deviation (s.t.d) of 0.6° . In contrast, the 90° rotated dihedral shows less stability in its calibrated polarimetric phase difference compared to the 0° rotated dihedral. Specifically, the s.t.d for the 90° rotated dihedral increases significantly to 12.3° , and its mean value shifts to -29.6° . The additional phase offset occurred on the dihedral with $\theta_{r}=90^{\circ}$ is due to the RCS reduction under yaw misalignment error as shown in Fig. 24. Such RCS reduction can lead to lower SNR and bring additional phase noise to the measurement.

Conclusion

This study presents a detailed investigation into the effects of misalignment errors, specifically yaw and pitch deviations, on the scattering response of dihedral reflectors in mm-wave polarimetric MIMO automotive radar. Simulations and measurements at 77 GHz revealed significant RCS variations, with changes up to 30 dB observed within small misalignment ranges ($0^{o}-2^{o}$). Misalignment effects were less pronounced when the dihedral was oriented at specific angles ($\theta_r=0^{o}$ for yaw and $\theta_r=90^{o}$ for pitch), offering configurations for stable calibration setups. To achieve stable RCS under misalignment conditions, a dihedral with dimensions w=135 mm and l=50 mm is recommended when pitch or yaw misalignment can be controlled within 1°. For larger misalignment angles, more robust configurations such as w=135 mm and l=100 mm or l=130 mm are preferred.

The analysis highlighted the trade-off between dihedral size and sensitivity to misalignment. Larger dihedrals provide stronger reflections but are more sensitive to misalignment compared to smaller ones, emphasizing the importance of selecting dimensions that balance RCS strength and stability.

Additionally, near-field effects were shown to influence calibration, with the largest RCS discrepancies between near- and far-field measurements occurring within $0^{o}-2^{o}$ yaw angles. The polarimetric calibration method proved to be effective for maintaining a stable phase response for a 0^{o} rotated dihedral, though increased phase variation was observed at $\theta_{r}=90^{o}$.

Acknowledgements. This research was supported by the National Growth Fund through the Dutch 6G flagship project "Future Network Services." The

authors would like to express their sincere gratitude to Pascal Aubry for his exceptional support in establishing the measurement environment and providing assistance with the measurements.

Declaration of interests. The authors report no conflict of interest.

References

- Wang W, Fang Z, Tang K, Wang X, Shu Z, Zhao Z and Zheng Y (2023) Wideband gain enhancement of MIMO antenna and its application in FMCW radar sensor integrated with CMOS-based transceiver chip for human respiratory monitoring. *IEEE Transactions on Antennas and Propagation* 71(1), 318–329.
- Abubakar HS, Zhao Z, Munir ME, Tareen WUK, Wang B, Kiani SH and Ali T (2024) Enhanced smartphone connectivity: Dual-band MIMO antenna with high isolation and low ECC. *Physica Scripta* 99(6), 065524.
- Munir ME, Nasralla MM and Farman H (2024) Design and development of super-compact millimeter wave antenna for future 5g vehicular applications. *IEEE 100th Vehicular Technology Conference (VTC2024-Fall)*. Washington, DC, USA. pp. 1–8.
- Munir ME, Nasralla MM and Esmail MA (2024) Four port tri-circular ring MIMO antenna with wide-band characteristics for future 5G and mmWave applications. Heliyon 10(8), e28714.
- Sethi WT, Kiani SH, Munir ME, Sehrai DA, Savci HS and Awan D (2024)
 Pattern diversity based four-element dual-band MIMO patch antenna for
 5g mmwave communication networks. *Journal of Infrared, Millimeter, and Terahertz Waves* 45(5), 521–537.
- Tinti A, Alfageme ST, Biarge SD and Pohl N (2023) ±45° linearly polarized PCB antennas for polarimetric automotive radar. *Photonics & Electromagnetics Research Symposium (PIERS)*. Prague: Czech Republic, pp. 571–577.
- Visentin T, Hasch J and Zwick T (2017) Calibration of a fully polarimetric 8×8 mimo fmcw radar system at 77 ghz. 11th European Conference on Antennas and Propagation (EUCAP), Paris, France. pp. 2530–2534.
- 8. Zhao C, Garcia-Tejero A, Bouwmeester W, Aslan Y, Krasnov O and Yarovoy A (2024) Calibration of polarimetric automotive radar with asymmetric MIMO topology and off-broadside beamforming. 2024 21st European Radar Conference (EuRAD), Paris, France. pp. 87–90.
- Palmer RD, Yeary MB, Schvartzman D, Salazar-Cerreno JL, Fulton C, McCord M, Cheong B, Bodine D, Kirstetter P, Sigmarsson HH, Yu T-Y, Zrnić D, Kelley R, Meier J and Herndon M (2023) Horus—a fully digital polarimetric phased array radar for next-generation weather observations. IEEE Transactions on Radar Systems 1 (1), 96–117.
- Fiorelli B, Arts M, Virone G, de Lera Acedo E and van Cappellen WA (2013) Polarization analysis and evaluation for radio astronomy aperture array antennas. 7th European Conference on Antennas and Propagation (EuCAP), Gothenburg, Sweden. pp. 461–465.
- Ferro-Famil L and Pottier E (2016). 2 SAR Imaging using Coherent Modes of Diversity: SAR Polarimetry, Interferometry and Tomography. Microwave Remote Sensing of Land Surface, (In Baghdadi N and Zribi M, Eds.), London, Oxford, United Kingdom: Elsevier, pp. 67–147.
- Visentin T, Hasch J and Zwick T (2017) Analysis of multipath and DOA detection using a fully polarimetric automotive radar. 2017 European Radar Conference (EURAD), Nuremberg, Germany. pp. 45–48.
- Tilly JF, Weishaupt F, Schumann O, Dickmann J and Wanielik G (2023) Road user detection on polarimetric pre-cfar radar data level. *IEEE Robotics and Automation Letters* 8(6), 3558–3565.
- 14. **Tilly JF, Schumann O, Weishaupt F, Dickmann J and Waniliek G** (2021) Polarimetric information representation for radar based road user detection with deep learning. *IEEE 24th International Conference on Information Fusion (FUSION)*, Sun City, South Africa. pp. 1–6.
- Tilly JF, Weishaupt F, Schumann O, Dickmann J and Wanielik G (2020)
 Road user classification with polarimetric radars. 17th European Radar
 Conference (EuRAD), Utrecht, Netherlands. pp. 112–115.

- Weishaupt F, Tilly JF, Dickmann J and Heberling D (2020) Polarimetric covariance gridmaps for automotive self-localization. *IEEE 23rd International Conference on Information Fusion (FUSION)*, Rustenburg, South Africa. pp. 1–8.
- 17. **Tinti A, Tejero Alfageme S, Duque Biarge S, Balcells-Ventura J and Pohl N** (2024) Fully polarimetric automotive radar: Proof of concept. *IEEE Transactions on Radar Systems* **2**, 645–660.
- Zhang G, Doviak RJ, Zrnic DS, Crain J, Staiman D and Al-Rashid Y (2009) Phased array radar polarimetry for weather sensing: A theoretical formulation for bias corrections. *IEEE Transactions on Geoscience and Remote Sensing* 47(11), 3679–3689.
- Petrov N, Yiğit E, Krasnov O and Yarovoy A (2022) Radar calibration by corner reflectors with mass-production errors. 18th European Radar Conference (EuRAD), London, United Kingdom. pp. 253–256.
- Weishaupt F, Tilly JF, Appenrodt N, Dickmann J and Heberling D
 (2022) Calibration and Signal Processing of Polarimetric Radar Data in Automotive Applications. Microwave Mediterranean Symposium (MMS), Pizzo Calabro, Italy. pp. 1–6.
- Wang S-Y and Jeng S-K (1998) A compact RCS formula for a dihedral corner reflector at arbitrary aspect angles. *IEEE Transactions on Antennas* and Propagation 46(7), 1112–1113.
- Liu J, Li T, Ma S, Wen Y, Xu Y and Nie G (2024) Analysis of the dihedral corner reflector's RCS features in multi-resource SAR. *Applied Sciences* 14(12), 5054.
- Ramesan R and Madathil D (2020) Modeling of radiation source using an equivalent dipole moment model. *Progress In Electromagnetics Research B* 89, 157–175.
- Yang X and Liu X (2021) Design of a wide-beam microstrip array antenna for automotive radar application. *IEEE Access* 9, 142340–142347.
- 25. **Zang Z, Zaman AU and Yang J** (2022) Single layer dual circularly polarized antenna array based on ridge gap waveguide for 77 ghz automotive radar. *IEEE Transactions on Antennas and Propagation* **70**(7), 5977–5982.
- 26. Ginsburg Brian P., Subburaj Karthik, Samala Sreekiran, Ramasubramanian Karthik, Singh Jasbir, Bhatara Sumeer, Murali Sriram, Breen Dan, Moallem Meysam, Dandu Krishnanshu, Jalan Saket, Nayak Neeraj P., Sachdev Rittu, Prathapan Indu, Bhatia Karan, Davis Tim, Seok Eunyoung, Parthasarathy Harikrishna, Chatterjee Rohit, Srinivasan Venkatesh, Giannini Vito, Kumar Anil, Kulak Ross, Ram Shankar, Gupta Pankaj, Parkar Zahir, Bhardwaj Sachin, Rakesh Y. C., Rajagopal K. A., Shrimali Arun, Rentala Vijay (2018) A multimode 76-to-81GHz automotive radar transceiver with autonomous monitoring. IEEE International Solid-State Circuits Conference (ISSCC), San Francisco, CA, USA. pp. 158–160.
- Huegel U and Garcia-Tejero A and Glogowski R and Willmann E and Pieper M and Merli F (2022) 3D waveguide metallized plastic antennas aim to revolutionize automotive radar. *Microwave Journal* 65(9).
- Garcia-Tejero A and Burgos-Garcia M and Merli F (2022) Highefficiency injection-molded waveguide horn antenna array for 76-81 GHz automotive radar applications. 19th European Radar Conference (EuRAD), Milan, Italy. pp. 21–24.



Changxu Zhao received the B.Sc. degree in Electrical Engineering and Intelligent Control from the Shanghai Maritime University, Shanghai, China, in 2020, and the B.Sc. degree in Engineering (Cum Laude) from the HZ University of Applied Sciences, Vlissingen, The Netherlands, in 2020. Afterward, he continued his master's studies at Delft University of Technology (TU Delft). In 2023, he completed his master's thesis (Cum Laude) and graduated from the Microwave Sensing, Signals

and Systems (MS3) group at TU Delft. In November 2023, he continued his research in the MS3 group as a Ph.D. candidate. His current research interests include polarimetric calibration and sensing in automotive radar applications.



Yanki Aslan received the B.Sc. degree with double specialization in communications and microwaves/antennas from the Department of Electrical and Electronic Engineering, Middle East Technical University, Ankara, Turkey, in 2014, and the M.Sc. (cum laude) and Ph.D. degrees (cum laude) in electrical engineering from Delft University of Technology, Delft, The Netherlands, in 2016 and 2020, respectively. Following his Postdoctoral Research with Delft University of

Technology in the Microwave Sensing, Signals and Systems (MS3) Group, he started as an Assistant Professor with TU Delft in April 2021. His current research interests include phased arrays for next-generation communication and sensing systems, array optimization, multibeam antennas, front-end architectures, and beamforming algorithms. Dr. Aslan was one of the recipients of the IEEE AP-S Doctoral Research Grant in 2018 and the EuMA Internship Award in 2019.



Alejandro Garcia-Tejero received the B.Sc. and M.Sc. degrees in telecommunications engineering from the Universidad Politécnica de Madrid, Spain, in 2016 and 2018, respectively. In 2017, he joined the École Fédérale de Lausanne, Lausanne, Switzerland as a Guest M.Sc. Student. He is currently working as an RF/Antenna Engineer with Huber+Suhner AG, Switzerland. His research interests include RF circuits, communication, and automotive radar antennas.



Wietse Bouwmeester received the B.Sc. degree in electrical engineering from the Delft University of Technology in 2016, and the M.Sc. degree in electrical engineering from the Delft University of Technology, with a focus on telecommunications and sensing systems. He graduated cum laude on the design of a conformal phased array antenna commissioned by ASTRON, the Dutch institute for radio astronomy. In May 2020, he joined the

Microwave Sensing, Signals, and Systems group of the TU Delft as a Ph.D. candidate, where he was working on polarimetric approaches to classify road surfaces and other targets with mm-wave radar for automotive applications. He obtained his doctoral degree in 2024.



Alexander Yarovoy received the Diploma (Hons.) in Radiophysics and Electronics from Kharkov State University, Ukraine, in 1984, and the Candidate and Doctor of Physics and Mathematical Sciences degrees in 1987 and 1994, respectively. He joined Kharkov State University as a Researcher in 1987, becoming a Full Professor in 1997. From 1994 to 1996, he was a Visiting Researcher at the Technical University of Ilmenau, Germany. Since 1999, he has been with Delft

University of Technology, The Netherlands, where he chairs the Microwave Sensing, Systems and Signals Group. He has authored over 500 scientific papers, seven patents, and 15 book chapters. His research interests include high-resolution radar, microwave imaging, and UWB antennas. He received the European Microwave Week Radar Awards in 2001 and 2012 and the ACES Best Paper Award in 2010. He has also held leadership roles in major conferences and served as an editor for prominent journals.